

Generative quantum machine learning via denoising diffusion probabilistic models

Bingzhi Zhang,^{1,2} Peng Xu,³ Xiaohui Chen,^{4,*} and Quntao Zhuang^{2,1,†}

¹*Department of Physics and Astronomy, University of Southern California, Los Angeles, California 90089, USA*

²*Ming Hsieh Department of Electrical and Computer Engineering,*

University of Southern California, Los Angeles, California 90089, USA

³*Department of Statistics, University of Illinois at Urbana-Champaign, Champaign, IL 61820, USA*

⁴*Department of Mathematics, University of Southern California, Los Angeles, California 90089, USA*

Deep generative models are key-enabling technology to computer vision, text generation and large language models. Denoising diffusion probabilistic models (DDPMs) have recently gained much attention due to their ability to generate diverse and high-quality samples in many computer vision tasks, as well as to incorporate flexible model architectures and relatively simple training scheme. Quantum generative models, empowered by entanglement and superposition, have brought new insight to learning classical and quantum data. Inspired by the classical counterpart, we propose the *quantum denoising diffusion probabilistic models* (QuDDPM) to enable efficiently trainable generative learning of quantum data. QuDDPM adopts sufficient layers of circuits to guarantee expressivity, while introduces multiple intermediate training tasks as interpolation between the target distribution and noise to avoid barren plateau and guarantee efficient training. We demonstrate QuDDPM’s capability in learning correlated quantum noise model and learning topological structure of nontrivial distribution of quantum data.

Artificial intelligence (AI) and quantum information science and engineering (QISE) are two rapidly growing areas of research in the past decade. QISE has revolutionized our understanding of performance limits in sensing [1, 2], communication [3, 4] and computing [5–9]. At the same time, AI deep learning has made numerous breakthroughs such as AlphaFold for accurate protein folding [10], Stable Diffusion for high-quality text-to-image generation [11], and more recently GPT models for synthesizing human-like dialogues. Currently, deep generative models form a key-enabling technology to generate new samples that empower impactful applications such as drug discovery [12], image reconstruction [13, 14] and text generation from large language models [15].

Quantum machine learning is an emergent area in the intersection between AI and QISE. Early works [16] have considered fault-tolerant quantum computers to enable speed up in machine learning tasks such as support-vector machine [17] and principal component analysis [18]. With near-term quantum devices, variational parameterized quantum circuits (PQC) are proposed to complete versatile tasks [19], in analogue to classical neural networks [20–22]. Besides solving classical problems, recent works also propose to learn quantum data with enhanced performance [21, 23–29].

In terms of generative models, quantum machine learning has brought advantage in Bayesian network [30], variational autoencoder (VAE) [31], Boltzmann machine [32] and general graph models [33]. In analogy to classical generative adversarial networks (GAN) [34], Refs. [35–37] provide a framework of quantum generative adversarial networks (QuGANs) applicable to both quantum and classical data [38, 39]. Despite the success, GAN models

are known for training issues such as mode collapse, i.e., unstable training and less diversity in generated data. In classical deep learning, denoising diffusion probabilistic models (DDPMs) and their close relatives [40–44] have recently gained much attention due to their ability to generate diverse and high-quality samples in many computer vision tasks [45–48] over the best GANs, as well as to incorporate flexible model architectures and relatively simple training scheme without adversarial training. Specifically, forward diffusion process (i.e., encoder) first gradually converts the observed data to a simple random noise (usually Gaussian) based on non-equilibrium thermodynamics, and then an associated time-reversal process (i.e., decoder) is learned to generate samples with target distribution from the noise [40–43].

In this work, we propose the *quantum denoising diffusion probabilistic models* (QuDDPM) to reap the benefit of their classical counterparts. Our QuDDPM provides an efficiently trainable scheme to generative quantum learning, through a coordination between a forward noisy diffusion process via quantum scrambling and a backward denoising process via quantum measurement. We demonstrate QuDDPM’s capability in learning correlated noise model for characterizing quantum device and learning topological structure of nontrivial quantum data. For an n -qubit problem, QuDDPM adopts linear-in- n layers of circuits to guarantee expressivity, while introduces $T \sim n/\log(n)$ intermediate training tasks interpolating the target distribution and to avoid barren plateau and guarantee efficient training.

I. GENERAL FORMULATION OF QUDDPM

We consider the task of the generating new elements from an unknown distribution \mathcal{E}_0 of quantum states, provided only a number of samples $\mathcal{S}_0 = \{|\psi_k\rangle\} \sim \mathcal{E}_0$ from

* xiaohuic@usc.edu

† qzhuang@usc.edu

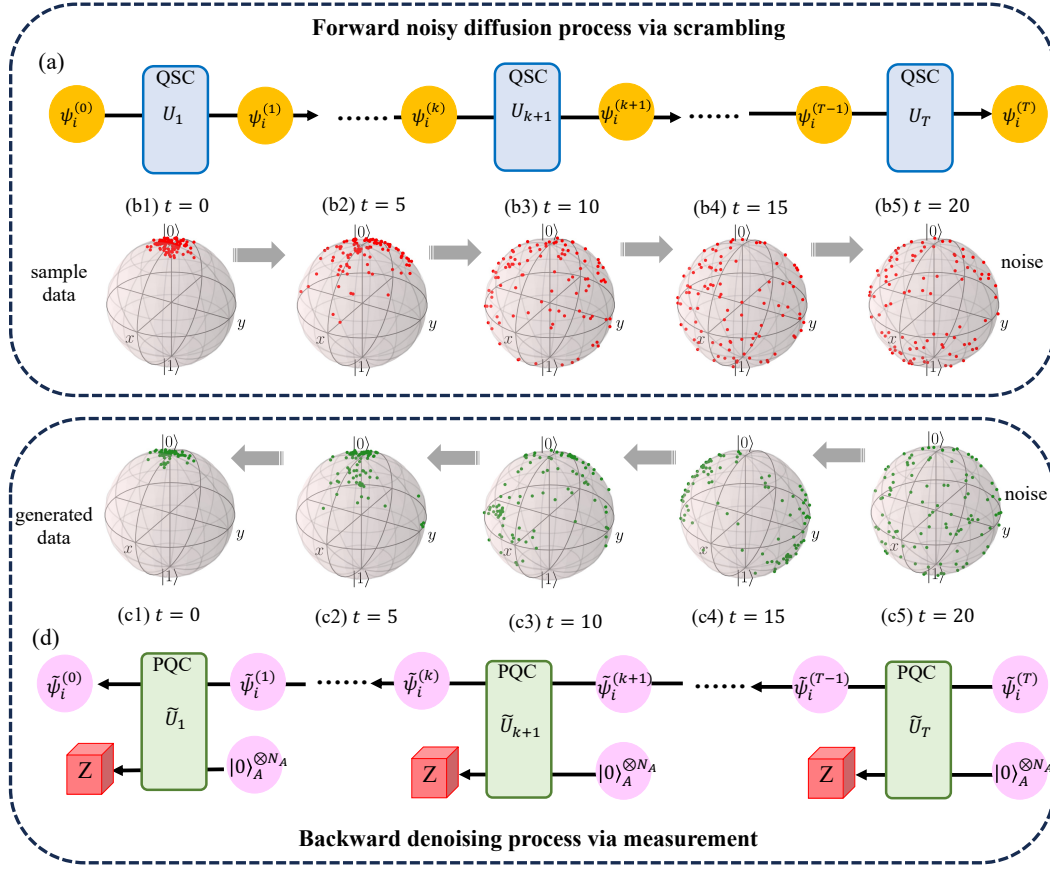


Figure 1. Schematic of QuDDPM. The forward noisy process is implemented by quantum scrambling circuit (QSC) in (a), while in the backward denoising process is achieved via measurement enabled by ancilla and PQC in (d). Subplots (b1)-(b5) and (c1-c4) presents the Bloch sphere dynamics in generation of states clustering around $|0\rangle$. The diffusion process consists of $T = 20$ steps. The backward PQC is applied on $n = 1$ data and $n_A = 1$ ancilla qubits with $L = 4$ layers. The size of data set is $N_{tr} = N_{te} = 100$. In (b) and (c), we consider data in the form of $|\psi^{(0)}\rangle \sim |0\rangle + \epsilon c_1 |1\rangle$ up to a normalization constant where $\text{Re}\{c_1\}, \text{Im}\{c_1\} \sim \mathcal{N}(0, 1)$ is Gaussian distributed and the scale factor is chosen $\epsilon = 0.08$.

the distribution. Such a state generation task appears in various applications. For example, when a quantum device experiences random coherent errors, it produces a distribution of quantum states in a computation. Learning the potentially correlated and complex coherent errors in a multi-qubit system is important for quantum device calibration, benchmark and testing, and has recently received much attention [49, 50]. Another example is when quantum sensor networks [24, 25] send quantum probes to obtain information about unitary physical process, on the return side the receiver will collect a pure state from a distribution in the ideal case. Furthermore, the distribution can also be quantum states encoding classical data, then the task also relates to the generation of classical data. We emphasize that the task under consideration—generating individual states from the distribution (e.g., a single Haar random state)—is *not* equivalent to generating the average state of a distribution (e.g., a fully mixed state for Haar ensemble) considered in QuGAN [35].

To complete the task, QuDDPM learns a map from

a noisy unstructured distribution of states to a structured target distribution \mathcal{E}_0 . It does so via a divide-and-conquer strategy of creating smooth interpolations between the target distribution and the full noisy distribution, so that the training is divided to sub-tasks of low-depth circuit to avoid barren plateau [51–54].

As shown in Fig. 1, QuDDPM includes two quantum circuits, one to enable the forward diffusion of sample data towards noise via scrambling and one to realize the backward denoising from noise towards generated data via measurement. For each data $|\psi_i^{(0)}\rangle$, the forward scrambling circuit (Fig. 1a) samples a series of T random unitary gates U_1, \dots, U_T , such that the state being generated $|\psi_i^{(k)}\rangle = \prod_{\ell=1}^k U_\ell |\psi_i^{(0)}\rangle$ evolves towards a fully scrambled random quantum state $|\psi_i^{(T)}\rangle$. Therefore, the ensemble $\mathcal{S}_k = \{|\psi_i^{(k)}\rangle\}_i$ evolves from the sample data towards a random ensemble of pure states from $k = 0$ to $k = T$. A Bloch sphere visualization of such a forward scrambling dynamics is depicted in Fig. 1(b1-b5) for a toy problem of learning single-qubit states clustered

around a single pure state e.g. $|0\rangle$ (see full details in later sections). At time $t = 0$ (b1), the sample data \mathcal{S}_0 cluster around the north pole of $|0\rangle$ state; After five steps of small random rotations, the states \mathcal{S}_4 spread out towards a larger volume at $t = 5$ (b2); At $t = T = 20$, the accumulation of the random rotations fully scramble the states to a noisy ensemble \mathcal{S}_T , randomly occupying the Bloch sphere uniformly (b5).

The forward noisy diffusion process creates an interpolation between the structured sample data \mathcal{S}_0 and the fully noisy data \mathcal{S}_T which enables the backward denoising process to be trained efficiently. Essentially, the backward process can start from randomly sampled noise $\tilde{\mathcal{S}}_T$ (Fig. 1c5) and reduce the noise gradually via measurement, towards the final generated data $\tilde{\mathcal{S}}_0$ (Fig. 1c1) that mimic the sample data (Fig. 1b1). Measurements are necessary, as the denoising map needs to be contractive that does not preserve the distance between states, yet we need to maintain the purity of each generated data in $\tilde{\mathcal{S}}_0$. Indeed, conditioned on the measurement results, the states remain pure throughout the dynamics, while the entropy of the state ensembles can in general decrease due to projective measurement.

As shown in Fig. 1d, each denoising step adopts a unitary \tilde{U}_k on n_A number of ancilla qubits in $|0\rangle$ and performs a projective measurement (in computational bases without loss of generality) on the ancilla after the unitary \tilde{U}_k . Starting from the state $|\tilde{\psi}_i^{(T)}\rangle$, which is randomly sampled from entire noise, each unitary plus measurement step evolves the random state towards the generated data $|\tilde{\psi}_i^{(0)}\rangle$. Note that here all unitaries \tilde{U}_k are fixed after training. In practice, the generation of the fully noisy state $|\tilde{\psi}_i^{(T)}\rangle$ can also be directly completed by running the T layers of forward scrambling circuit on a fixed initial state. Therefore, to generate an n -qubit random quantum state stratifying the target distribution that \mathcal{S}_0 represents, one runs the forward diffusion on an arbitrary state and then runs the backward denoising to end up at the final state.

Now we discuss about the number of local gates required for the QuDDPM algorithm to generate an n -qubit random quantum state stratifying the target distribution that \mathcal{S}_0 represents, while the cost of training will be discussed in the next section. For simplicity, we assume the qubits are one-dimensional and only have nearest neighbor interactions, while similar counting can be done for higher connectivity cases. To guarantee good performance of erasing any information from the initial distribution, the forward scrambling circuits needs number of layers linear in n as predicted by t -design [55, 56]. Consequently, the total number of gates in this forward diffusion will be $O(n^2)$, despite the different grouping into T steps of unitaries U_k . Indeed, we expect the increase of T to guarantee the efficiency of training, as we show in Appendix explicitly. In special cases, where controlled diffusion is possible due to symmetry, we can reduce the number of gates, which will be explored in fu-

ture work. The backward circuit will be similar, with at most $n_A \leq 2n$ additional ancillas, as $2n$ ancilla suffices for general quantum channel. Therefore the number of gates in the T steps is also $O(n^2)$, leading to the overall gate complexity of QuDDPM to be $O(n^2)$ to generate an n -qubit target random quantum state.

II. TRAINING OF THE QUDDPM

A. Training strategy

In classical DDPM, the Gaussian nature of the diffusion allows efficient training via maximizing an evidence lower bound (ELBO) for the log-likelihood function (see details in Appendix). Refs. [40, 41] showed that the ELBO can be expressed as a linear combination of (relative) entropy terms for Gaussian distributions that can be evaluated *analytically*. However, in QuDDPM, we do not expect such analytical simplification to exist at all—what can be implemented efficiently on a quantum device cannot be efficiently simulated on a classical computer, and therefore we do not expect any efficient classical description of the dynamics. Instead, the training of the QuDDPM relies on the capability of quantum measurements to extract information about ensemble of quantum states for the efficient evaluation of a cost function. Due to measurement destructing quantum states, each training also require running the quantum circuit from the initial sample that are assumed to be generated on-demand.

The training of the QuDDPM with T forward and background steps consists of T training cycles, starting from the first denoising step \tilde{U}_T towards the last denoising step \tilde{U}_1 . As shown in Fig. 2, at the training cycle $(T + 1 - k)$, the forward noisy diffusion process is implemented from U_1 to U_k to generates the noisy ensemble $\mathcal{S}_k = \{|\psi_i^{(k)}\rangle\}_i$. While the backward denoising process performs the denoising steps \tilde{U}_T to \tilde{U}_{k+1} to generate the denoising ensemble $\tilde{\mathcal{S}}_k = \{|\tilde{\psi}_i^{(k)}\rangle\}_i$. Within the training cycle, the parameters of the denoising PQC \tilde{U}_{k+1} is updated such that the generated denoising ensemble $\tilde{\mathcal{S}}_k$ converges to the noisy ensemble \mathcal{S}_k . Therefore, QuDDPM divides the original training problem into T smaller ones, such that each training task is relatively easy. Indeed, even with a global cost function, as long as each \tilde{U}_{k+1} has order $\log(n)$ layers of gates, one can still avoid barren plateau [52]. Therefore, we can divide the $\Omega(n)$ layers (required by approximating t -design in forward scrambling) of gates to $T \in \Omega(n/\log n)$ diffusion steps to enable efficient training.

B. Cost function

To enable the training, we introduce a loss function $\mathcal{L}(\mathcal{S}_k, \tilde{\mathcal{S}}_k)$ to quantify the distance between the two dis-

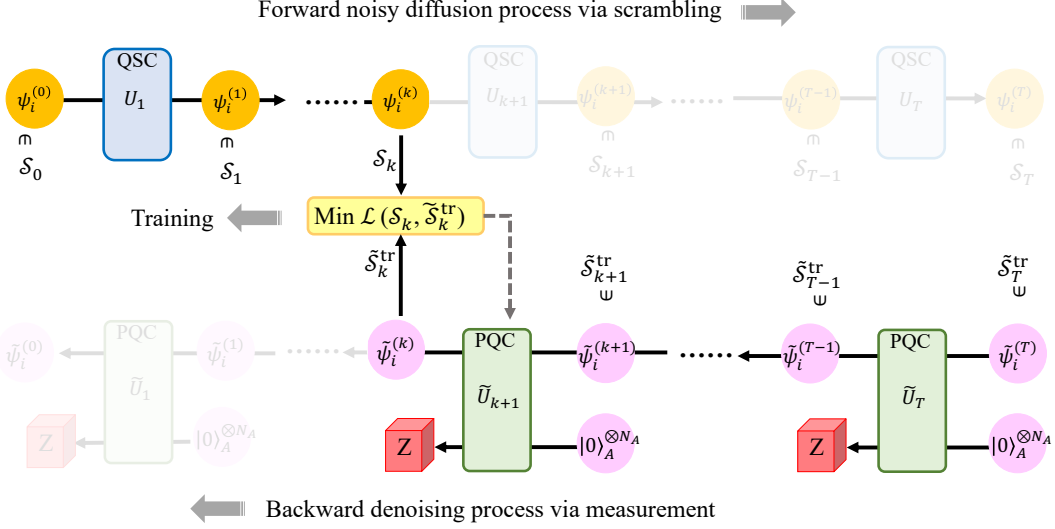


Figure 2. The training of QuDDPM at each step $t = k$. Pairwise distance between states in generated ensemble $\tilde{\psi}_i^{(k)} \in \mathcal{S}_k^{\text{tr}}$ and true diffusion ensemble $\psi_j^{(k)} \in \mathcal{S}_k$ is measured and utilized in the evaluation of the loss function \mathcal{L} .

tribution of quantum states. In this work, we focus on the Maximum Mean Discrepancy (MMD) [57] and the Wasserstein distance [58, 59] based on the state overlaps $|\langle \psi_i^{(k)} | \tilde{\psi}_i^{(k)} \rangle|^2$, which can be estimated via a swap test (see Appendix). We note that QuDDPM can also function with other choices of loss function.

Given two independent distributions of pure states \mathcal{E}_1 and \mathcal{E}_2 on the state vector space V . The *state-wise fidelity* between $|\psi\rangle$ and $|\phi\rangle$ is defined as $F(|\phi\rangle, |\psi\rangle) = |\langle \phi | \psi \rangle|^2$, and we can further define the *mean fidelity* as

$$\bar{F}(\mathcal{E}_1, \mathcal{E}_2) = \mathbb{E}_{|\phi\rangle \sim \mathcal{E}_1, |\psi\rangle \sim \mathcal{E}_2} [|\langle \phi | \psi \rangle|^2], \quad (1)$$

where the random states $|\phi\rangle \sim \mathcal{E}_1$ and $|\psi\rangle \sim \mathcal{E}_2$ are drawn independently. Since the fidelity F is a symmetric and positive definite quadratic kernel, according to the theory of reproducing kernel Hilbert space (RKHS), there exists a unique Hilbert space $\mathcal{H} := \mathcal{H}(F)$ of real-valued functions on V with the reproducing kernel $F(|\phi\rangle, |\psi\rangle) = |\langle \phi | \psi \rangle|^2$ such that we can embed the state vectors as elements of \mathcal{H} (cf. Appendix for more details of the kernel embedding). Based on the kernel F , the (squared) MMD loss function is defined as

$$\begin{aligned} \mathcal{L}_{\text{MMD}}(\mathcal{E}_1, \mathcal{E}_2) \\ := \sup_{g \in \mathcal{B}} \left| \mathbb{E}_{|\phi\rangle \sim \mathcal{E}_1} [F(\cdot, |\phi\rangle)] - \mathbb{E}_{|\psi\rangle \sim \mathcal{E}_2} [F(\cdot, |\psi\rangle)] \right|^2, \end{aligned} \quad (2)$$

where \mathcal{B} is the unit ball in \mathcal{H} centered at the origin and $\langle \cdot, \cdot \rangle_{\mathcal{H}}$ denotes the inner product in the RKHS. In Appendix, we show that

$$\mathcal{L}_{\text{MMD}}(\mathcal{E}_1, \mathcal{E}_2) = \bar{F}(\mathcal{E}_1, \mathcal{E}_1) + \bar{F}(\mathcal{E}_2, \mathcal{E}_2) - 2\bar{F}(\mathcal{E}_1, \mathcal{E}_2), \quad (3)$$

which allows the estimation of MMD through sampled state ensembles \mathcal{S}_1 and \mathcal{S}_2 . It is clear that the expressivity of MMD as a statistical distance measure depends on the richness of the function class \mathcal{B} (and thus the kernel F). On one hand, \mathcal{H} should be rich enough to ensure the identifiability, i.e., $\mathcal{L}_{\text{MMD}}(\mathcal{E}_1, \mathcal{E}_2) = 0$ if and only if $\mathcal{E}_1 = \mathcal{E}_2$. On the other hand, \mathcal{H} needs to be reasonably large to ensure the quality of statistical estimation of the resulting MMD with finite sample size of state ensembles. Hence, whether fidelity (1) is a proper kernel choice is problem-dependent. For instance, we consider a circular uniform on the Bloch sphere and the Haar random state distributions. The following Lemma 1 shows that the MMD between these two state distributions is zero, thus implying the fidelity kernel F cannot distinguish them. Thus, a proper choice of distance measure between distributions of quantum states is important for achieving good performance of QuDDPM.

Lemma 1 *Let \mathcal{E}_1 be a uniform circular distribution on the Bloch sphere and \mathcal{E}_2 be the Haar random state distribution. Then $\mathcal{L}_{\text{MMD}}(\mathcal{E}_1, \mathcal{E}_2) = 0$.*

In the case of complex distributions of quantum states where the MMD fails to characterize their difference, we may alternatively consider the Wasserstein distance, a geometrically meaningful distance for comparing complex data distributions based on the theory of optimal transport [58]. In a nutshell, optimal transport aims to find the most cost-efficient way for transporting a source probability distribution \mathcal{E}_1 to a target probability distribution \mathcal{E}_2 . In the context of quantum states, a natural choice of the cost function is the quantum trace distance $D(|\phi\rangle, |\psi\rangle)$ on V [59]. For pure states, D reduces to a function of infidelity $D^2(|\phi\rangle, |\psi\rangle) = 1 - |\langle \phi | \psi \rangle|^2$. Then

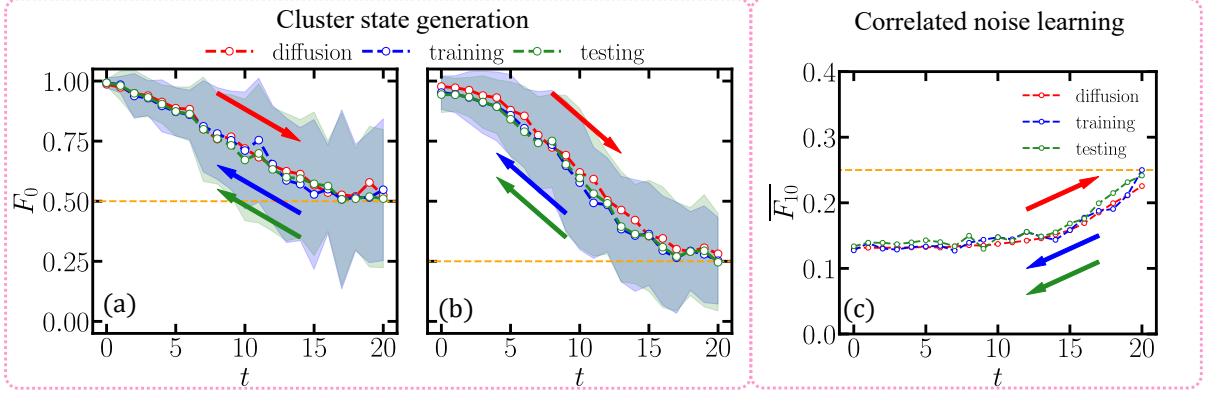


Figure 3. Fidelity dynamics in generation of states clustering around $|0\rangle^{\otimes n}$ in (a), (b), and generation of states with probabilistic correlated noise on a specific qubit state in (c). In the cluster state generation, the backward PQC is applied on $n_A = 1$ ancilla qubit and (a) $n = 1$ qubits with $L = 4$ and (b) $n = 2$ qubits with $L = 6$. Average fidelity \overline{F}_0 between states at step t and $|0\rangle^{\otimes n}$ for forward diffusion (red), backward training (blue), backward test (green) are plotted. The shaded areas in blue and green show the sample standard deviation for backward training and test. The size of training and test data sets are both $N_{\text{tr}} = N_{\text{te}} = 100$. At $t = 0$, the ensemble average fidelity $\overline{F}_0 = 0.987 \pm 0.013, 0.992 \pm 0.021, 0.993 \pm 0.014$ for diffusion, training and testing with (a) 1-qubit and $\overline{F}_0 = 0.977 \pm 0.014, 0.952 \pm 0.070, 0.944 \pm 0.075$ for diffusion, training and testing with (b) 2-qubit. The corresponding Bloch sphere dynamics of diffusion and testing for (a) are shown in Fig. 1(b1)-(b5) and (c5)-(c1). In (a), the clustered data are same as in Fig. 1(b),(c). In (b), the data in the form of $|\psi^{(0)}\rangle \sim |0, 0\rangle + \epsilon(c_1|0, 1\rangle + c_2|1, 0\rangle + c_3|1, 1\rangle)$ up to a normalization constant where $\{c_i\}_{i=1}^3$ are all complex Gaussian distributed and the scale factor is chosen $\epsilon = 0.06$. In the generation of states with probabilistic correlated noise, the PQC is applied on $n_A = 2$ ancilla qubits and $n = 2$ data qubits with $L = 6$. The noise perturbation range is $\delta \in [-\pi/3, \pi/3]$. Average fidelity \overline{F}_{10} between states at step t and $|1, 0\rangle$ for forward diffusion (red), backward training (blue), backward test (green) are plotted. Through optimization the generated ensemble averaged fidelity reaches $\overline{F}_{10} = 0.128, 0.133$ for training and test compared to the theoretical prediction of $p|c_1|^2 \mathbb{E}_\delta[\sin^2 \delta] = 0.129$. In all cases, the number of diffusion steps is $T = 20$, and backward PQC is trained with MMD distance.

Kantorovich's formulation for optimal transportation is to solve the following optimization problem

$$\text{OPT} := \min_{\pi \in \Pi(\mathcal{E}_1, \mathcal{E}_2)} \int_{V \times V} D^p(|\phi\rangle, |\psi\rangle) d\pi(|\phi\rangle, |\psi\rangle) \quad (4)$$

for $p \geq 1$, where $\Pi(\mathcal{E}_1, \mathcal{E}_2)$ is the set of admissible *transport plans* (i.e., *couplings*) of probability distributions on $V \times V$ such that $\pi(B \times V) = \mathcal{E}_1(B)$ and $\pi(V \times B) = \mathcal{E}_2(B)$ for any measurable $B \subset V$; namely $\Pi(\mathcal{E}_1, \mathcal{E}_2)$ stands for all distributions with marginals as \mathcal{E}_1 and \mathcal{E}_2 . The Kantorovich problem in (4) induces a metric, known as the *p-Wasserstein distance*, on the space $\mathcal{P}_p(V)$ of probability distributions on V with finite p -th moment. In particular, the p -Wasserstein distance $W_p(\mathcal{E}_1, \mathcal{E}_2) = \text{OPT}^{1/p}$, and it has identifiability in the sense that $W_p(\mathcal{E}_1, \mathcal{E}_2) = 0$ if and only if $\mathcal{E}_1 = \mathcal{E}_2$. More details can be found in Appendix.

III. APPLICATIONS OF QUDDPM

Now we consider some generative learning applications to showcase QuDDPM. Towards this goal, we consider a particular realization of QuDDPM with each unitary U_k and \tilde{U}_k implemented by the fast scrambling model [60] and hardware efficient ansatz separately (see Appendix). To test the performance after training, we randomly sample N_{test} random noise states, and perform the optimized

backward PQC to generate the sampled data and evaluate the cost functions along the backward steps.

A. Clustered states generation: learning the errors

When a real quantum device is programmed to generate a quantum state, it inevitably suffers from errors in the gate control parameters. As a result, the states generated S_0 are close to the target state but has nontrivial coherent errors. Learning the clustered states therefore helps us understand errors of quantum devices. We begin with the simplest single-qubit scenario and define the target state as $|0\rangle$ to demonstrate QuDDPM.

In the single-qubit scenario, the forward scrambling process only consists of single qubit rotations, where each angle is randomly sampled, e.g., from the uniform distribution $U[-\pi/8, \pi/8]$. With independent sampling, each data undergoes a unique scrambling process. When T is large enough, the sample data \mathcal{S}_T at the end of forward scrambling will be uniformly distributed on the Bloch sphere, approaching the Haar random distribution. In Fig. 1(b1)-(b5), we show a Bloch sphere visualization on the forward scrambling process of a $N_{\text{tr}} = 100$ training data set.

In the backward training process, we start from $N_{\text{tr}} = 100$ single-qubit Haar random states generated by a single-qubit random rotation. As shown in Fig. 1(d), each

backward denoising step involves training a PQC acting on the single data qubit and $n_A = 1$ ancilla qubits, with a Pauli- Z measurement on the ancilla to reduce the noise. Step-wise training with a MMD cost function in (3) recovers the clustered ensemble via the steps of Fig. 1(c5) through (c1) as expected.

To understand the performance more directly, besides the cost function, we can utilize the overlap fidelity F_0 with the state $|0\rangle$ due to the clustering of the targeted data. In Fig. 3(a), we plot the training and testing results. The average fidelity of the ensemble in the forward noisy diffusion process is depicted in red dots. At time $t = 0$, the fidelity is close to unity by construction; while the noisy diffusion decreases the fidelity gradually, towards the Haar random value of average fidelity $\bar{F}_0 = 1/2$ at $t = 20$. The backward denoising begins at $t = 20$, with Haar random average fidelity $\bar{F}_0 = 1/2$. Via the step-wise training, we recover the original distribution towards $t = 0$, which is verified by the increase of average fidelity towards unity (blue dots). The blue shaded region shows the sample fluctuation, which decreases to small value at the end of the training at $t = 0$ as well. To test the optimized QuDDPM circuit, we then generate random test samples and input them to the backward denoising circuits and indeed observe similar increase of fidelity towards $t = 0$. Due to finite sample and finite training steps, the converged average fidelity $\bar{F}_0 = 0.992 \pm 0.021$ in training and $\bar{F}_0 = 0.993 \pm 0.014$ in testing.

The above task can be extended to multiple qubits. We consider an distribution of two-qubit states clustered around $|0,0\rangle$ for simplicity. Despite the lack of a Bloch sphere to visualize as in Fig. 1, we plot the average fidelity with the state $|0,0\rangle$ in Fig. 3(b) and the same performance is confirmed for the QuDDPM. Note that the Haar average of fidelity is now $1/4$ due to the increased dimension.

To further connect to testing quantum devices, we consider the task of learning correlated noises, where each Pauli-string of error \mathbf{P} happen according to a nontrivial joint distribution. We take a two-qubit example of fully correlated noise and demonstrate QuDDPM's capability in capturing the noise statistics. Specifically, we consider an error model where fully correlated XX rotations $e^{-i\delta X_1 X_2}$ happen on the two qubits with probability p and fully correlated ZZ rotations $e^{-i\delta Z_1 Z_2}$ happen with probability $1 - p$. In each case, the angle of rotation δ is uniformly sampled from the range $[-\delta_0, \delta_0]$. When starting from any fixed pure state, this error model leads to a clustered state distribution with nontrivial correlation. To test the QuDDPM, we pick an initial state $|\Psi\rangle = c_0|00\rangle + c_1|01\rangle + c_3|11\rangle$ where c_0, c_1, c_3 are fixed complex numbers and consider the distribution of states generated by the fully correlated noise model above. As the $|10\rangle$ component in the superposition only appears when XX error happens, we can utilize average fidelity $\bar{F}_{10} = \mathbb{E}_{\tilde{\psi}_0} |\langle 10 | \psi^{(0)} \rangle|^2$ as the performance metric to estimate the error probability p that describes the correlated noise, $\hat{p} = \bar{F}_{10} / (|c_1|^2 \mathbb{E}_{\delta} [\sin^2 \delta])$. We show a nu-

merical example in Fig. 3(c), where the generated ensemble average fidelity is $\bar{F}_{10} = 0.128$ and $\bar{F}_{10} = 0.133$ in training and testing, compared to theoretical prediction $p|c_1|^2 \mathbb{E}_{\delta} [\sin^2 \delta] = 0.129$. The testing samples has a slightly larger deviation due to a finite sample size in training; while the training convergence is excellent.

B. Nontrivial topology: learning the structure

While the previous applications have the states clustered around a single state, now we consider general distributions of states with nontrivial topology to further test the capability of QuDDPM. As an example, we consider states generated by applying a unitary on a single state (chosen as $|0\rangle$ without loss of generality),

$$|\psi_i\rangle = U(\mathbf{x}_i) |0\rangle. \quad (5)$$

This also models the scenario where one solves a classical generative task using QuDDPM—the classical data \mathbf{x}_i is encoded onto the quantum data via a parameterized unitary $U(\mathbf{x}_i)$. A common choice of encoding in machine learning [38, 61–63] is $U(\mathbf{x}) = e^{-i\mathbf{x} \cdot \mathbf{G}}$, where the unitaries share a common generator \mathbf{G} in a tensor product form to enable efficient implementation. Such a choice of unitaries generate a ring structure in the Hilbert space and creates a different challenge from the clustered data case.

We test QuDDPM with a single qubit toy example, where the generators are chosen as Pauli- Y and the rotation angles uniform in $[0, 2\pi)$. In the QuDDPM training, we use the Wasserstein distance [59] to cope with the nontrivial topology. The forward noisy diffusion process on the sample data and the backward denoising process for training and testing are depicted in Fig. 4. In subplots (a1-a5), the initial ring of data (red) gradually spreads over the Bloch sphere, while the backward evolution maps the random noise towards the ring of data (blue) up to a precision as shown in (b5-b1). To avoid over-fitting, we also run the backward process with independent test data and observe similar convergence. To quantitatively evaluate the performance of QuDDPM, we evaluate the deviation by Pauli- Y expectation $\langle Y \rangle^2$. As shown in Fig. 4(d) red dots, the forward noisy diffusion drives the sample data from the initial zero $\langle Y^2 \rangle$ towards the distribution average $\overline{\langle Y \rangle^2} = 1/3$ as predicted by the Haar random value. Conversely, the backward denoising process continuously deviates from the Haar value of $1/3$ towards the zero value of the true distribution, as shown in the blue dots. The same can be observed for the test data as depicted in green in Fig. 4(e). Due to finite data sample and finite amount of training steps, the converged training has deviations from the perfect zero y component at $\overline{\langle Y \rangle^2} = 0.00367 \pm 0.0251, 0.00506 \pm 0.0439$ for training and testing.

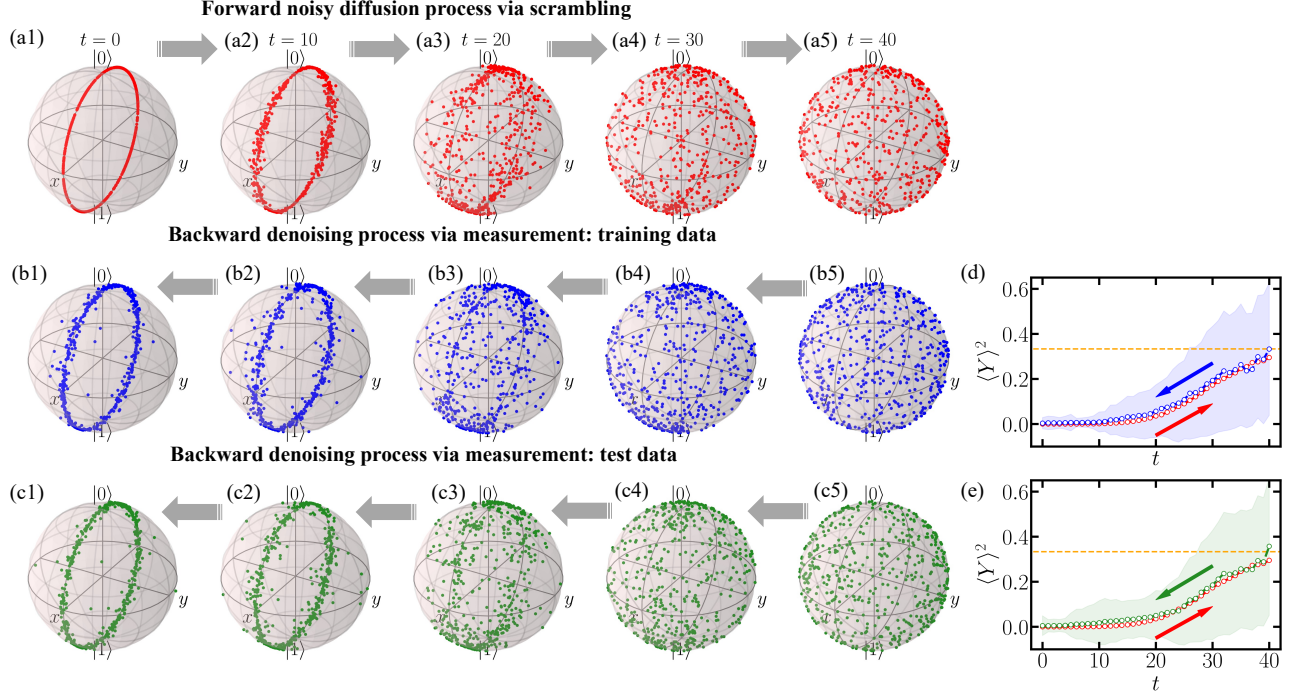


Figure 4. Bloch visualization of the forward (a1-a5) and backward (b1-b5, c1-c5) process. (d)(e) deviation of generated states from unit circle in $X - Z$ plane. The diffusion process consists of $T = 40$ steps. The backward PQC is applied on $n = 1$ data and $n_A = 2$ ancilla qubits with $L = 6$ layers, trained via Wasserstein distance. The deviation $\langle Y \rangle^2$ for forward diffusion (red), backward training (blue), backward test (green) are plotted. The shaded area show the sample standard deviation. The size of training and test data sets are both $N_{tr} = N_{te} = 500$. At $t = 0$, the ensemble average deviation is $\overline{\langle Y \rangle^2} = 0.00367 \pm 0.0251, 0.00506 \pm 0.0439$ for training and testing.

IV. DISCUSSION

In this work, we propose QuDDPM to solve quantum generative tasks with guaranteed efficient training. Below, we discuss about several related works. Ref. [64] utilizes diffusion map (DM) for unsupervised learning of topological phases and [65] proposes a diffusion K -means manifold clustering approach based on the diffusion distance [66]. Quantum DM algorithm has also been considered [67] for potentially quantum speed-up. However, these works are not on generative learning and do not consider any denoising process. Layer-wise training [68] also attempts to divide a training problem into sub-tasks in non-generative learning; however, the performance of such strategies is limited [69]. QuDDPM integrates the division of training task and an actual noisy diffusion

process to enable provable benefit in training.

Finally, we point out some future directions. Our current QuDDPM architecture requires a loss function based on fidelity estimations. For large systems, fidelity estimation can be challenging to implement. Towards efficient training in large systems, alternative loss functions can be adopted. For example, one may consider adopting another quantum circuit trained for telling the ensembles apart, such as quantum convolutional neural network [22] and other circuit architecture [70]. Such an approach will combine QuDDPM and the adversarial agent in QuGAN to resolve training problem in QuGAN. Another future direction is controlled diffusion [71]: when the ensemble has special symmetry, one can restrict the forward scrambling, the backward denoising and the random noise ensemble to that symmetry.

[1] V. Giovannetti, S. Lloyd, and L. Maccone, Phys. Rev. Lett. **96**, 010401 (2006).
[2] Z. Zhang and Q. Zhuang, Quantum. Sci. Technol. **6**, 043001 (2021).
[3] F. Xu, X. Ma, Q. Zhang, H.-K. Lo, and J.-W. Pan, Rev. Mod. Phys. **92**, 025002 (2020).
[4] S. Hao, H. Shi, W. Li, J. H. Shapiro, Q. Zhuang, and

Z. Zhang, Phys. Rev. Lett. **126**, 250501 (2021).
[5] P. Shor, SIAM J. Comput. **26**, 1484 (1997).
[6] E. Farhi, J. Goldstone, S. Gutmann, J. Lapan, A. Lundgren, and D. Preda, Science **292**, 472 (2001).
[7] A. W. Harrow, A. Hassidim, and S. Lloyd, Phys. Rev. Lett. **103**, 150502 (2009).
[8] F. G. Brandão, A. Kaveh, T. Li, C. Y.-Y. Lin, K. M.

- Svore, and X. Wu, arXiv:1710.02581 (2017).
- [9] A. J. Daley, I. Bloch, C. Kokail, S. Flannigan, N. Pearson, M. Troyer, and P. Zoller, *Nature* **607**, 667 (2022).
 - [10] J. Jumper, R. Evans, A. Pritzel, T. Green, M. Figurnov, O. Ronneberger, K. Tunyasuvunakool, R. Bates, A. Židek, A. Potapenko, A. Bridgland, C. Meyer, S. A. A. Kohl, A. J. Ballard, A. Cowie, B. Romera-Paredes, S. Nikolov, R. Jain, J. Adler, T. Back, S. Petersen, D. Reiman, E. Clancy, M. Zielinski, M. Steinegger, M. Pacholska, T. Berghammer, S. Bodenstein, D. Silver, O. Vinyals, A. W. Senior, K. Kavukcuoglu, P. Kohli, and D. Hassabis, *Nature* **596**, 583 (2021).
 - [11] R. Rombach, A. Blattmann, D. Lorenz, P. Esser, and B. Ommer, High-resolution image synthesis with latent diffusion models (2021), arXiv:2112.10752 [cs.CV].
 - [12] N. Anand, R. Eguchi, I. I. Mathews, C. P. Perez, A. Derry, R. B. Altman, and P.-S. Huang, *Nat. Commun.* **13**, 746 (2022).
 - [13] C. Saharia, J. Ho, W. Chan, T. Salimans, D. J. Fleet, and M. Norouzi, arXiv:2104.07636 (2021).
 - [14] R. A. Yeh, C. Chen, T. Y. Lim, A. G. Schwing, M. Hasegawa-Johnson, and M. N. Do, in *2017 IEEE Conference on Computer Vision and Pattern Recognition, CVPR 2017, Honolulu, HI, USA, July 21-26, 2017* (IEEE Computer Society, 2017) pp. 6882–6890.
 - [15] H. Touvron, T. Lavril, G. Izacard, X. Martinet, M.-A. Lachaux, T. Lacroix, B. Rozière, N. Goyal, E. Hambro, F. Azhar, A. Rodriguez, A. Joulin, E. Grave, and G. Lample, Llama: Open and efficient foundation language models (2023), arXiv:2302.13971 [cs.CL].
 - [16] J. Biamonte, P. Wittek, N. Pancotti, P. Rebentrost, N. Wiebe, and S. Lloyd, *Nature* **549**, 195 (2017).
 - [17] P. Rebentrost, M. Mohseni, and S. Lloyd, *Phys. Rev. Lett.* **113**, 130503 (2014).
 - [18] S. Lloyd, M. Mohseni, and P. Rebentrost, *Nat. Phys.* **10**, 631 (2014).
 - [19] M. Cerezo, A. Arrasmith, R. Babbush, S. C. Benjamin, S. Endo, K. Fujii, J. R. McClean, K. Mitarai, X. Yuan, L. Cincio, *et al.*, *Nature Reviews Physics* **3**, 625 (2021).
 - [20] N. Killoran, T. R. Bromley, J. M. Arrazola, M. Schuld, N. Quesada, and S. Lloyd, *Phys. rev. res.* **1**, 033063 (2019).
 - [21] A. Abbas, D. Sutter, C. Zoufal, A. Lucchi, A. Figalli, and S. Woerner, *Nat. Comput. Sci* **1**, 403 (2021).
 - [22] I. Cong, S. Choi, and M. D. Lukin, *Nat. Phys.* **15**, 1273 (2019).
 - [23] H.-Y. Huang, M. Broughton, J. Cotler, S. Chen, J. Li, M. Mohseni, H. Neven, R. Babbush, R. Kueng, J. Preskill, *et al.*, *Science* **376**, 1182 (2022).
 - [24] Q. Zhuang and Z. Zhang, *Phys. Rev. X* **9**, 041023 (2019).
 - [25] Y. Xia, W. Li, Q. Zhuang, and Z. Zhang, *Phys. Rev. X* **11**, 021047 (2021).
 - [26] H.-Y. Huang, M. Broughton, M. Mohseni, R. Babbush, S. Boixo, H. Neven, and J. R. McClean, *Nature Commun.* **12**, 2631 (2021).
 - [27] L. Banchi, J. Pereira, and S. Pirandola, *PRX Quantum* **2**, 040321 (2021).
 - [28] M. C. Caro, H.-Y. Huang, N. Ezzell, J. Gibbs, A. T. Sornborger, L. Cincio, P. J. Coles, and Z. Holmes, *Nat. Commun.* **14**, 3751 (2023).
 - [29] V. Gebhart, R. Santagati, A. A. Gentile, E. M. Gauger, D. Craig, N. Ares, L. Banchi, F. Marquardt, L. Pezzè, and C. Bonato, *Nat. Rev. Phys.* **5**, 141 (2023).
 - [30] X. Gao, E. R. Anschuetz, S.-T. Wang, J. I. Cirac, and M. D. Lukin, *Phys. Rev. X* **12**, 021037 (2022).
 - [31] A. Khoshaman, W. Vinci, B. Denis, E. Andriyash, H. Sadeghi, and M. H. Amin, *Quantum. Sci. Technol.* **4**, 014001 (2018).
 - [32] M. H. Amin, E. Andriyash, J. Rolfe, B. Kulchytskyy, and R. Melko, *Phys. Rev. X* **8**, 021050 (2018).
 - [33] X. Gao, Z.-Y. Zhang, and L.-M. Duan, *Sci. Adv.* **4**, eaat9004 (2018).
 - [34] I. Goodfellow, J. Pouget-Abadie, M. Mirza, B. Xu, D. Warde-Farley, S. Ozair, A. Courville, and Y. Bengio, in *Adv. Neural Inf. Process.*, Vol. 27, edited by Z. Ghahramani, M. Welling, C. Cortes, N. Lawrence, and K. Weinberger (Curran Associates, Inc., 2014).
 - [35] S. Lloyd and C. Weedbrook, *Phys. Rev. Lett.* **121**, 040502 (2018).
 - [36] P.-L. Dallaire-Demers and N. Killoran, *Phys. Rev. A* **98**, 012324 (2018).
 - [37] L. Hu, S.-H. Wu, W. Cai, Y. Ma, X. Mu, Y. Xu, H. Wang, Y. Song, D.-L. Deng, C.-L. Zou, *et al.*, *Sci. Adv.* **5**, eaav2761 (2019).
 - [38] H.-L. Huang, Y. Du, M. Gong, Y. Zhao, Y. Wu, C. Wang, S. Li, F. Liang, J. Lin, Y. Xu, *et al.*, *Phys. Rev. Appl* **16**, 024051 (2021).
 - [39] E. Y. Zhu, S. Johri, D. Bacon, M. Esencan, J. Kim, M. Muir, N. Murgai, J. Nguyen, N. Piseni, A. Schouela, *et al.*, *Phys. rev. res.* **4**, 043092 (2022).
 - [40] J. Sohl-Dickstein, E. Weiss, N. Maheswaranathan, and S. Ganguli, in *International conference on machine learning* (PMLR, 2015) pp. 2256–2265.
 - [41] J. Ho, A. Jain, and P. Abbeel, *Adv. Neural Inf. Process.* **33**, 6840 (2020).
 - [42] Y. Song, J. Sohl-Dickstein, D. P. Kingma, A. Kumar, S. Ermon, and B. Poole, in *International Conference on Learning Representations* (2021).
 - [43] A. Schneuing, Y. Du, C. Harris, A. Jamasb, I. Igashov, W. Du, T. Blundell, P. Lió, C. Gomes, M. Welling, M. Bronstein, and B. Correia, Structure-based drug design with equivariant diffusion models (2022), arXiv:2210.13695 [q-bio.BM].
 - [44] Y. Chen, T. T. Georgiou, and M. Pavon, *Journal of Optimization Theory and Applications* **169**, 671 (2016).
 - [45] P. Dhariwal and A. Nichol, *Adv. Neural Inf. Process.* **34**, 8780 (2021).
 - [46] G. Müller-Franzes, J. M. Niehues, F. Khader, S. T. Arasteh, C. Haarbuerger, C. Kuhl, T. Wang, T. Han, S. Nebelung, J. N. Kather, *et al.*, arXiv preprint arXiv:2212.07501 (2022).
 - [47] A. Jalal, M. Arvinte, G. Daras, E. Price, A. G. Dimakis, and J. Tamir, in *Adv. Neural Inf. Process.*, Vol. 34, edited by M. Ranzato, A. Beygelzimer, Y. Dauphin, P. Liang, and J. W. Vaughan (Curran Associates, Inc., 2021) pp. 14938–14954.
 - [48] Y. Song and S. Ermon, in *Adv. Neural Inf. Process.*, Vol. 32, edited by H. Wallach, H. Larochelle, A. Beygelzimer, F. d'Alché-Buc, E. Fox, and R. Garnett (Curran Associates, Inc., 2019).
 - [49] R. Harper, S. T. Flammia, and J. J. Wallman, *Nat. Phys.* **16**, 1184 (2020).
 - [50] S. Chen, Y. Liu, M. Otten, A. Seif, B. Fefferman, and L. Jiang, *Nat. Commun.* **14**, 52 (2023).
 - [51] J. R. McClean, S. Boixo, V. N. Smelyanskiy, R. Babbush, and H. Neven, *Nat. Commun.* **9**, 4812 (2018).
 - [52] M. Cerezo, A. Sone, T. Volkoff, L. Cincio, and P. J. Coles, *Nat. Commun.* **12**, 1791 (2021).

- [53] S. Wang, E. Fontana, M. Cerezo, K. Sharma, A. Sone, L. Cincio, and P. J. Coles, Nat. Commun. **12**, 6961 (2021).
- [54] C. Ortiz Marrero, M. Kieferová, and N. Wiebe, PRX Quantum **2**, 040316 (2021).
- [55] F. G. Brandao, A. W. Harrow, and M. Horodecki, Commun. Math. Phys. **346**, 397 (2016).
- [56] A. W. Harrow and S. Mehraban, Commun. Math. Phys., 1 (2023).
- [57] A. Gretton, K. M. Borgwardt, M. J. Rasch, B. Schölkopf, and A. Smola, J. Mach. Learn. Res. **13**, 723 (2012).
- [58] C. Villani, *Topics in Optimal Transportation*, Graduate studies in mathematics (American Mathematical Society, 2003).
- [59] O. Oreshkov and J. Calsamiglia, Phys. Rev. A **79**, 032336 (2009).
- [60] R. Belyansky, P. Bienias, Y. A. Kharkov, A. V. Gorshkov, and B. Swingle, Phys. Rev. Lett. **125**, 130601 (2020).
- [61] V. Havlíček, A. D. Córcoles, K. Temme, A. W. Harrow, A. Kandala, J. M. Chow, and J. M. Gambetta, Nature **567**, 209 (2019).
- [62] M. Schuld, arXiv preprint arXiv:2101.11020 (2021).
- [63] G. Li, R. Ye, X. Zhao, and X. Wang, Adv. Neural Inf. Process. **35**, 19456 (2022).
- [64] J. F. Rodriguez-Nieva and M. S. Scheurer, Nat. Phys. **15**, 790 (2019).
- [65] X. Chen and Y. Yang, Appl. Comput. Harmon. Anal. **52**, 303 (2021).
- [66] R. R. Coifman and S. Lafon, Appl. Comput. Harmon. Anal. **21**, 5 (2006), special Issue: Diffusion Maps and Wavelets.
- [67] A. Sornsaeng, N. Dangniam, P. Palittapongarnpim, and T. Chotibut, Phys. Rev. A **104**, 052410 (2021).
- [68] A. Skolik, J. R. McClean, M. Mohseni, P. van der Smagt, and M. Leib, Quantum. Mach. **3**, 1 (2021).
- [69] E. Campos, D. Rabinovich, V. Akshay, and J. Biamonte, Phys. Rev. A **104**, L030401 (2021).
- [70] B. Zhang and Q. Zhuang, Quantum. Sci. Technol. **7**, 035017 (2022).
- [71] Y. Song, L. Shen, L. Xing, and S. Ermon, arXiv:2111.08005 (2021).
- [72] T. Hsing and R. Eubank, *Theoretical Foundations of Functional Data Analysis, with an Introduction to Linear Operators*, Wiley Series in Probability and Statistics (Wiley, 2015).
- [73] G. Peyré and M. Cuturi, Foundations and Trends in Machine Learning **11**, 355 (2019).
- [74] S. Chakrabarti, H. Yiming, T. Li, S. Feizi, and X. Wu, Adv. Neural Inf. Process. **32** (2019).
- [75] G. De Palma, M. Marvian, D. Trevisan, and S. Lloyd, IEEE Trans. Inf. Theory **67**, 6627 (2021).
- [76] B. T. Kiani, G. De Palma, M. Marvian, Z.-W. Liu, and S. Lloyd, Quantum. Sci. Technol. **7**, 045002 (2022).
- [77] J. A. Smolin and D. P. DiVincenzo, Phys. Rev. A **53**, 2855 (1996).
- [78] S.-X. Zhang, J. Allcock, Z.-Q. Wan, S. Liu, J. Sun, H. Yu, X.-H. Yang, J. Qiu, Z. Ye, Y.-Q. Chen, *et al.*, Quantum **7**, 912 (2023).
- [79] J. R. Johansson, P. D. Nation, and F. Nori, Comput. Phys. Commun. **183**, 1760 (2012).
- [80] R. Flamary, N. Courty, A. Gramfort, M. Z. Alaya, A. Boisbunon, S. Chambon, L. Chapel, A. Corenflos, K. Fatras, N. Fournier, L. Gautheron, N. T. Gayraud, H. Janati, A. Rakotomamonjy, I. Redko, A. Rolet,

A. Schutz, V. Seguy, D. J. Sutherland, R. Tavenard, A. Tong, and T. Vayer, J. Mach. Learn. Res. **22**, 1 (2021).

Appendix A: Backgrounds

1. Classical DDPM

Classical DDPM can be viewed as a latent variational autoencoder (VAE) model with stochastic hidden layers of the same dimension as the input data. The forward diffusion process simply adds a sequence of small amount of Gaussian perturbations to the data sample x_0 in T steps to produce the noisy samples x_1, \dots, x_T according to a linear Markov chain:

$$q(x_t | x_{t-1}) = N(x_t | \sqrt{1 - \beta_t}x_{t-1}, \beta_t I),$$

where $\beta_t \in (0, 1)$ is a noise schedule such that $q(x_t)$ converges to $N(0, I)$. Usually the noise schedule satisfies $\beta_1 < \beta_2 < \dots < \beta_T$ so that larger step sizes are used when the samples become more noisy. In the time-reversal process, we would like to sample from $q(x_{t-1} | x_t)$, which allows us to generate new data sample from the noise distribution $q(x_T)$. However, the conditional distribution $q(x_{t-1} | x_t)$ is intractable and approximated by a decoder of the form:

$$p_\theta(x_{t-1} | x_t) = N(x_{t-1} | \mu_\theta(x_t, t), \sigma_t^2 I),$$

where the time-dependent conditional mean vector μ_θ is parameterized by a neural network. Then the training of μ_θ can be efficiently performed by maximizing an evidence lower bound (ELBO) for the log-likelihood function $\log p_\theta(x_0)$. Refs. [40, 41] showed that the ELBO can be expressed as a linear combination of (relative) entropy terms for Gaussian distributions that can be evaluated analytically into a simple weighted L^2 loss function.

2. Reproducing kernel Hilbert spaces and maximum mean discrepancy

A bivariate function $F : V \times V \rightarrow \mathbb{R}$ is a positive definite kernel if $\sum_{i,j=1}^m c_i c_j F(|\phi\rangle_i, |\phi\rangle_j) \geq 0$ for all $m \geq 1$, $|\phi\rangle_1, \dots, |\phi\rangle_m \in V$, and $c_1, \dots, c_m \in \mathbb{R}$. From the Moore-Aronszajn theorem (see e.g., [72, Theorem 7.2.4]), for every symmetric and positive-definite kernel F , there is a unique Hilbert space $\mathcal{H} := \mathcal{H}(F)$ of real-valued functions on V such that:

- (i) $F(\cdot, |\phi\rangle) \in \mathcal{H}$ for each $|\phi\rangle \in V$;
- (ii) $g(|\phi\rangle) = \langle g, F(\cdot, |\phi\rangle) \rangle_{\mathcal{H}}$ for each $g \in \mathcal{H}$ and $|\phi\rangle \in V$.

The space \mathcal{H} of functions $\{g : V \rightarrow \mathbb{R}\}$ is called the reproducing kernel Hilbert space (RKHS) associated with the kernel F . Property (i) defines a feature map (a.k.a. RKHS map) $V \rightarrow \mathcal{H}$ via $|\phi\rangle \mapsto F(\cdot, |\phi\rangle)$, and property

(ii) is the reproducing kernel property for the evaluation functionals. In addition, we have for all $|\phi\rangle, |\psi\rangle \in V$,

$$F(|\phi\rangle, |\psi\rangle) = \langle F(\cdot, |\psi\rangle), F(\cdot, |\phi\rangle) \rangle_{\mathcal{H}}.$$

Based on the kernel F , the (squared) maximum mean discrepancy (MMD) loss between two state distributions is defined in Eq. (2). By duality of \mathcal{H} , we have

$$\begin{aligned} \mathcal{L}_{\text{MMD}}(\mathcal{E}_1, \mathcal{E}_2) &= \left\| \mathbb{E}_{|\phi\rangle \sim \mathcal{E}_1} [F(\cdot, |\phi\rangle)] - \mathbb{E}_{|\psi\rangle \sim \mathcal{E}_2} [F(\cdot, |\psi\rangle)] \right\|_{\mathcal{H}}^2. \end{aligned}$$

Therefore, we may calculate the MMD loss as following

$$\begin{aligned} \mathcal{L}_{\text{MMD}}(\mathcal{E}_1, \mathcal{E}_2) &= \langle \mathbb{E}_{|\phi\rangle \sim \mathcal{E}_1} [F(\cdot, |\phi\rangle)], \mathbb{E}_{|\phi'\rangle \sim \mathcal{E}_1} [F(\cdot, |\phi'\rangle)] \rangle_{\mathcal{H}} \\ &\quad + \langle \mathbb{E}_{|\psi\rangle \sim \mathcal{E}_2} [F(\cdot, |\psi\rangle)], \mathbb{E}_{|\psi'\rangle \sim \mathcal{E}_2} [F(\cdot, |\psi'\rangle)] \rangle_{\mathcal{H}} \\ &\quad - 2 \langle \mathbb{E}_{|\phi\rangle \sim \mathcal{E}_1} [F(\cdot, |\phi\rangle)], \mathbb{E}_{|\psi\rangle \sim \mathcal{E}_2} [F(\cdot, |\psi\rangle)] \rangle_{\mathcal{H}} \\ &= \mathbb{E}_{|\phi\rangle, |\phi'\rangle \sim \mathcal{E}_1} [F(|\phi\rangle, |\phi'\rangle)] \\ &\quad + \mathbb{E}_{|\psi\rangle, |\psi'\rangle \sim \mathcal{E}_2} [F(|\psi\rangle, |\psi'\rangle)] \\ &\quad - 2 \mathbb{E}_{|\phi\rangle \sim \mathcal{E}_1, |\psi\rangle \sim \mathcal{E}_2} [F(|\phi\rangle, |\psi\rangle)], \end{aligned}$$

where all random states $|\phi\rangle, |\phi'\rangle, |\psi\rangle, |\psi'\rangle$ are drawn independently. Hence, we have established the connection

$$\mathcal{L}_{\text{MMD}}(\mathcal{E}_1, \mathcal{E}_2) = \overline{F}(\mathcal{E}_1, \mathcal{E}_1) + \overline{F}(\mathcal{E}_2, \mathcal{E}_2) - 2\overline{F}(\mathcal{E}_1, \mathcal{E}_2),$$

where $\overline{F}(\mathcal{E}_1, \mathcal{E}_2) := \mathbb{E}_{|\phi\rangle \sim \mathcal{E}_1, |\psi\rangle \sim \mathcal{E}_2} [F(|\phi\rangle, |\psi\rangle)]$. In particular, if $F = |\langle \phi | \psi \rangle|^2$ is state-wise fidelity, then the resulting MMD corresponds to the mean fidelity defined in Eq. (1).

3. Computation of Wasserstein distance

In the discrete or empirical cases, where \mathcal{S}_1 and \mathcal{S}_2 are supported over finite number of state vectors $\{|\phi_i\rangle\}_{i=1}^m$ and $\{|\psi_j\rangle\}_{j=1}^n$, computation of Wasserstein distance can be cast into a linear program [73]. To this end, let a and b be histograms representing \mathcal{S}_1 and \mathcal{S}_2 , respectively. Define the $m \times n$ cost matrix C by $C_{i,j} := D^2(|\phi_i\rangle, |\psi_j\rangle)$, where $|\phi_i\rangle$ and $|\psi_j\rangle$ are state vectors from sampled ensemble state \mathcal{S}_1 and \mathcal{S}_2 , respectively. For pure states, the cost matrix reduces to a function of infidelity, i.e., $C_{i,j} = 1 - F^2(|\phi_i\rangle, |\psi_j\rangle)$. Then we have

$$\begin{aligned} W_2(\mathcal{S}_1, \mathcal{S}_2) &= \min_P \langle P, C \rangle, \\ \text{s.t.} \quad &P \mathbf{1}_n = a, \\ &P^\top \mathbf{1}_m = b, \\ &P \geq 0. \end{aligned}$$

Furthermore, we note that the above generalization of Wasserstein distance to characterize separation between two ensembles of quantum states is different from the case of Refs. [74–76], where only a pair of quantum states are considered.

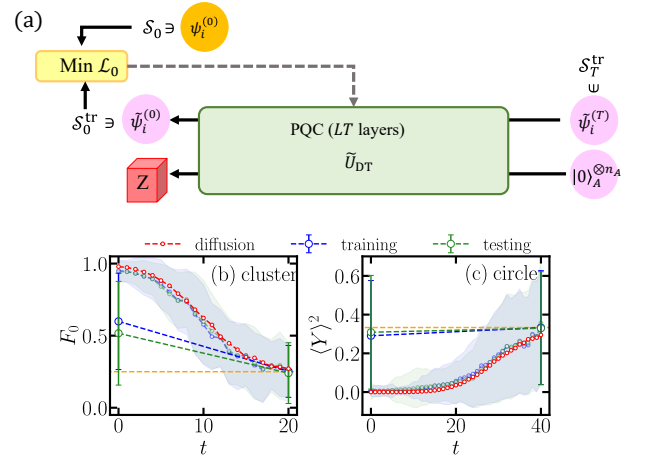


Figure 5. Schematic and performance of QuDT in state ensemble generation. Since the forward of QuDT only has a single step to noise, it is not necessary to implement. In backward process, there is also a single PQC \tilde{U}_{DT} with depth LT . In the training, the samples generated via applying \tilde{U}_{DT} on random states are directly compared to the target ensemble S_0 , shown in (a). In the bottom panel, we show the performance of QuDT to generate (b) clustered state around $|0, 0\rangle$ with $L_{DT} = 80$ and (c) circular state ensemble with $L_{DT} = 240$. Blue and green dots with error bar represents the mean and standard deviation of samples generated by QuDT in training and test. All other parameters and distance choice is same as the ones used in QuDDPM, see Fig. 3(b) and Fig. 4. The dotted line with shaded areas in background are QuDDPM performance in Fig. 3(b) and Fig. 4(d)(e) for comparison.

Appendix B: Comparison to quantum direct transport (QuDT)

Here we compare the performance between QuDDPM and quantum direct transport (QuDT). QuDT utilizes the same setup as QuDDPM, but attempts to generate the target state ensemble from a random state ensemble directly by only one PQC with L_{DT} layers (see Fig. 5(a)). Note that due to the single-step operation, the forward noisy diffusion process is not necessary to implement. For a fair comparison, the PQC in QuDT works on the same number of data and ancilla qubits and has the same total number of layers of circuits $L_{DT} = TL$ as the QuDDPM. The difference is that QuDDPM adopts forward diffusion combining backward denoising with T steps. We show the performance of QuDT in generating clustered and ring-structured state ensemble in Fig. 5(bottom). Compared to the performance of QuDDPM in Figs. 3 and 4, QuDT presents a much larger deviation to the target state ensemble in both cases, which indicates the necessity of having multiple denoising steps to improve the capability of QuDDPM. The minimum number of denoising steps to obtain the optimal performance, and the scaling of performance with respect to diffusion steps T are subject to future study.

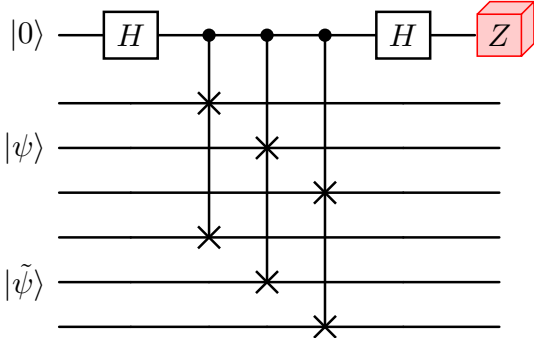


Figure 6. Circuit implementation of swap test. We show an example of swap test between two 3-qubit state $|\psi\rangle, |\tilde{\psi}\rangle$. A Z-basis measurement is performed at the end.

Appendix C: SWAP test

In the QuDDPM framework in the main text, we need to evaluate the fidelities between states $|\psi\rangle$ from real diffusion ensemble \mathcal{S}_k and the ones $|\tilde{\psi}\rangle$ from backward generated ensemble $\tilde{\mathcal{S}}_k$. For any two pure states $|\psi\rangle$ and $|\tilde{\psi}\rangle$, one can perform the SWAP test to obtain the fidelity, which is illustrated in Fig. 6. The SWAP test consists of two Hadamard gate and a controlled-swap gate applied on $2n + 1$ qubits. Given the input $|0, \psi, \tilde{\psi}\rangle$, the output state ahead of measurement is

$$|0, \psi, \tilde{\psi}\rangle \rightarrow \frac{1}{2} |0\rangle (|\psi, \tilde{\psi}\rangle + |\tilde{\psi}, \psi\rangle) + \frac{1}{2} |1\rangle (|\psi, \tilde{\psi}\rangle - |\tilde{\psi}, \psi\rangle), \quad (\text{C1})$$

then the probability of measure 0 on the first qubit is

$$\begin{aligned} P(\text{first qubit in } |0\rangle) &= \frac{1}{4} (\langle\psi, \tilde{\psi}| + \langle\tilde{\psi}, \psi|) (|\psi, \tilde{\psi}\rangle + |\tilde{\psi}, \psi\rangle) \\ &= \frac{1}{2} + \frac{1}{2} |\langle\psi|\tilde{\psi}\rangle|^2 \end{aligned} \quad (\text{C2})$$

which directly indicates the fidelity. To implement the swap test between two n -qubit state $|\psi\rangle$ and $|\tilde{\psi}\rangle$, in general we need n Fredkin gate between every pair of qubits of $|\psi\rangle$ and $|\tilde{\psi}\rangle$, where it is sufficient to implement a Fredkin gate among a control qubit and two target qubits via 5 two-qubit gate [77]. Therefore, in general $\mathcal{O}(5n)$ two-qubit gates are enough to perform the swap test in Fig. 6 regardless the locality of these gates.

Appendix D: Forward and backward circuits

The forward noisy process is implemented by the fast scrambling model [60] with controllable parameters on n data qubits to mimic the diffusion process in the Hilbert space. The diffusion circuit is implemented as (see Fig. 7

(a))

$$U(\phi_t, g_t) = \prod_{t=1}^T W_t(g_t) V_t(\phi_t), \quad (\text{D1})$$

where V_t consists of general single qubit rotations on each qubit as

$$V_t(\phi_t) = \bigotimes_{k=1}^n e^{-i\phi_{t,3k+2} Z_k/2} e^{-i\phi_{t,3k+1} Y_k/2} e^{-i\phi_{t,3k} Z_k/2}, \quad (\text{D2})$$

and homogeneous entangling layer W_t consists of ZZ rotation on every pair of qubits,

$$\begin{aligned} W_t(g_t) &= \exp \left[-i \frac{g_t}{2\sqrt{n}} \sum_{k_1 < k_2} Z_{k_1} Z_{k_2} \right] \\ &= \prod_{k_1 < k_2} \exp \left[-i \frac{g_t}{2\sqrt{n}} Z_{k_1} Z_{k_2} \right]. \end{aligned} \quad (\text{D3})$$

With a tunable range of random rotation angles ϕ and g , we can control the diffusion speed of original quantum states ensemble \mathcal{S}_0 in the Hilbert space towards Haar random states ensemble.

The backward denoising process consists of T steps, where the operation at every step is implemented by a PQC $\tilde{U}_t(\theta_t)$ followed by measurements on ancillae.

$$\begin{aligned} \Phi_t(|\tilde{\psi}^{(t)}\rangle) &= \frac{(\Pi_A \otimes \mathbf{I}_D) \tilde{U}_t |\tilde{\psi}^{(t)}\rangle}{\sqrt{\langle\tilde{\psi}^{(t)}| \tilde{U}_t^\dagger (\Pi_A \otimes \mathbf{I}_D) \tilde{U}_t |\tilde{\psi}^{(t)}\rangle}} \\ &= |\mathbf{z}(t)\rangle_A \otimes |\tilde{\psi}^{(t-1)}\rangle \end{aligned} \quad (\text{D4})$$

where $\Pi_A = |\mathbf{z}(t)\rangle\langle\mathbf{z}(t)|_A$ is the POVM of measurement on ancillas in computational basis $|\mathbf{z}(t)\rangle_A$. Note that we do not make any specific constraint on the measurement results $\mathbf{z}(t)$, instead, we simply perform the measurement on ancillas and collect post-measurement state on data qubits $|\tilde{\psi}^{(t-1)}\rangle$.

In general, the backward PQC can utilize any architecture as long as its expressivity can guarantee for the backward transport from ensemble \mathcal{S}_{t+1} to \mathcal{S}_t . In this work, we adopt the hardware-efficient ansatz which is universal and easy to implement in practical experiments. For a L -layer backward PQC \tilde{U}_t , in each layer it consists of single qubits rotations along X and Y axes on each qubit, followed by control-Z gate on nearest neighbors as (see Fig. 7 (b))

$$\tilde{U}_t(\theta_t) = \prod_{\ell=1}^L \tilde{W}_t \tilde{V}_t(\theta_t) \quad (\text{D5})$$

where

$$\tilde{V}_t(\theta_t) = \bigotimes_{k=1}^n e^{-i\theta_{t,2k+1} Y_k/2} e^{-i\theta_{t,2k} X_k/2} \quad (\text{D6})$$

$$\tilde{W}_t = \bigotimes_{k=1}^{\lfloor (n-1)/2 \rfloor} \text{CZ}_{2k,2k+1} \bigotimes_{k=1}^{\lfloor n/2 \rfloor} \text{CZ}_{2k-1,2k} \quad (\text{D7})$$

with CZ_{k_1, k_2} to be the control-Z gate on qubit k_1 and k_2 .

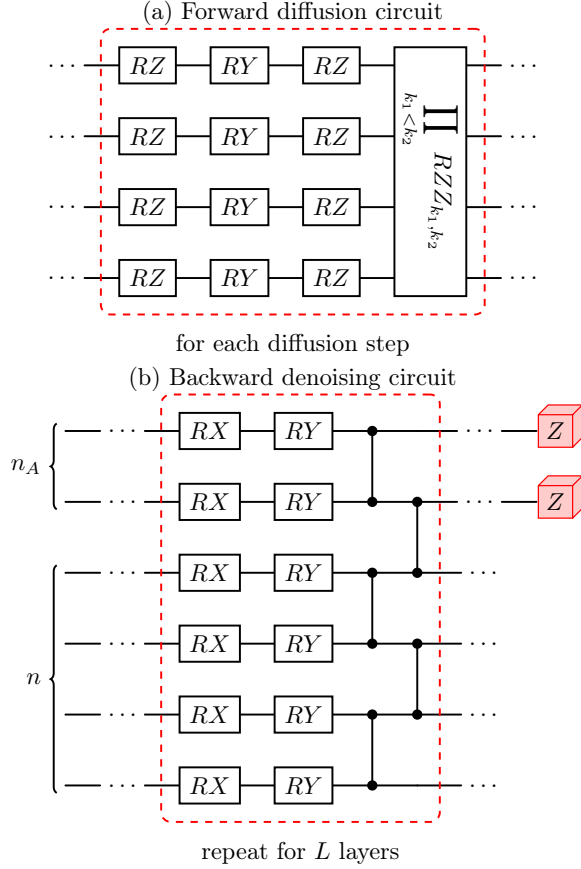


Figure 7. Quantum circuit architectures. In (a) we show the forward diffusion circuit for one diffusion step on a system of $n = 4$ qubits. In (b) we show one-layer architecture of a L -layer backward denoising PQC on a system of $n = 4$ data and $n_A = 2$ ancilla qubits. RX, RY and RZ are Pauli X, Y and Z rotations. RZZ is the two-qubit ZZ rotation.

The whole backward denoising process can thus be represented as

$$\Phi = \Phi_1 \circ \Phi_2 \circ \dots \circ \Phi_{T-1} \circ \Phi_T. \quad (\text{D8})$$

Appendix E: Additional details on distance metrics evaluation

In Fig. 8, we show a numerical comparison between the MMD distance (see Eq. 3) and Wasserstein distance (see Eq. 4) in different generation tasks. In the clustered state generation (Fig. 8(a), (b)), both distance measure behaves similarly. However, for the circular state generation in Fig. 8(c), (d), the Wasserstein distance can characterize the diffusion of ensemble while the MMD distance fails. Note that only relative shift of MMD or Wasserstein loss through diffusion matters, while a comparison between their magnitude is unfair. In the following, we provide the simple proof on Lemma 1.

Proof of Lemma 1. We can calculate the ensemble average fidelity by Haar integral as

$$\begin{aligned} \overline{F}(\mathcal{E}_1, \mathcal{E}_2) &= \frac{1}{2\pi} \int_0^{2\pi} d\theta \int dU |\langle 0|U^\dagger e^{-i\theta Y}|0\rangle|^2 \\ &= \frac{1}{2\pi} \int d\theta \frac{\text{tr}(|0\rangle\langle 0|) \text{tr}(e^{-i\theta Y} |0\rangle\langle 0| e^{i\theta Y})}{2} \\ &= \frac{1}{2}, \\ \overline{F}(\mathcal{E}_1, \mathcal{E}_1) &= \frac{1}{(2\pi)^2} \int_0^{2\pi} d\theta d\theta' |\langle 0|e^{i\theta' Y} e^{-i\theta Y}|0\rangle|^2 \\ &= \frac{1}{(2\pi)^2} \int_0^{2\pi} d\theta d\theta' \cos^2(\theta' - \theta) \\ &= \frac{1}{2}, \\ \overline{F}(\mathcal{E}_2, \mathcal{E}_2) &= \int dU dU' |\langle 0|U^\dagger U'|0\rangle|^2 \\ &= \int dU \frac{\text{tr}(|0\rangle\langle 0|) \text{tr}(U |0\rangle\langle 0| U^\dagger)}{2} \\ &= \frac{1}{2}. \end{aligned}$$

Therefore, the MMD distance is

$$\mathcal{L}_{\text{MMD}}(\mathcal{E}_1, \mathcal{E}_2) = \overline{F}(\mathcal{E}_1, \mathcal{E}_1) + \overline{F}(\mathcal{E}_2, \mathcal{E}_2) - 2\overline{F}(\mathcal{E}_1, \mathcal{E}_2) = 0, \quad (\text{E1})$$

which indicates its incapability to discriminate the difference between the circular state ensemble and Haar random states. ■

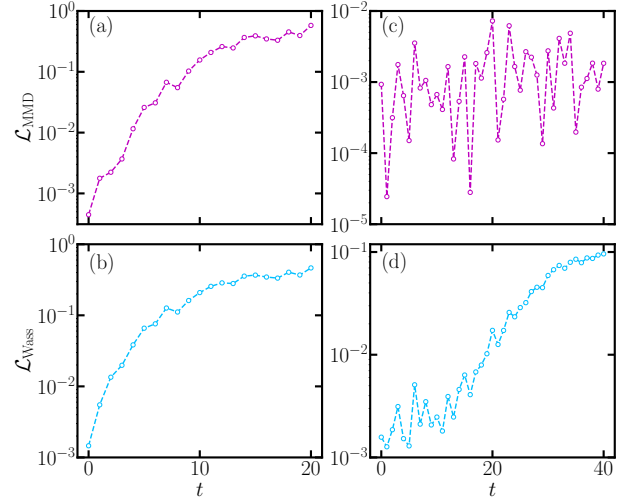


Figure 8. MMD and Wasserstein loss between ensemble S_0 and ensemble through diffusion process at step t , S_t in generation of cluster state (left) and circular state ensemble (right). For cluster state ensemble, MMD (a) and Wasserstein loss (c) behaves similarly. For circular state ensemble, MMD loss (c) vanishes while Wasserstein loss characterizes the diffusion of distribution. The data set size for cluster states is $|\mathcal{S}| = 100$, and $|\mathcal{S}| = 500$ for circular states.

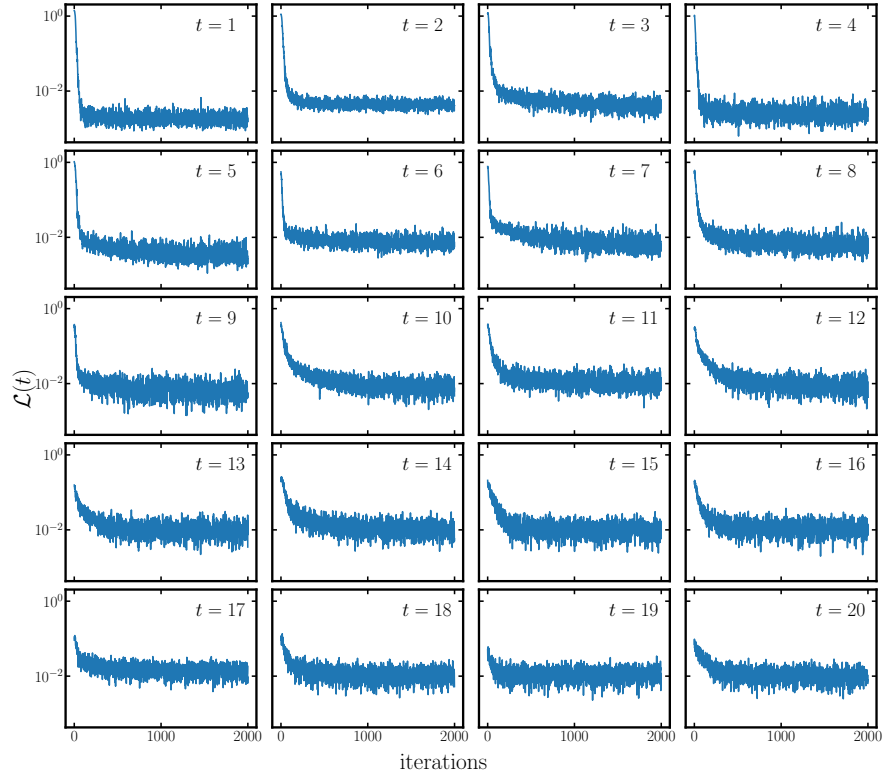


Figure 9. Training history of loss function in each denoising step for generating cluster state ensemble close to $|0,0\rangle$. The backward PQC is the same as in Fig. 3 (b).

For the true distribution, when $\mathcal{E}_1 = \mathcal{E}_2$, we should have $\mathcal{L}_{\text{MMD}}(\mathcal{E}_1, \mathcal{E}_2) = \mathcal{L}_{\text{Wass}}(\mathcal{E}_1, \mathcal{E}_2) = 0$ in theory, while in practice due to finite samples, both of them cannot vanish exactly (see Fig. 8) left with a relatively small residual.

Appendix F: Details of training

In this work, the simulation of QuDDPM is implemented with the Python library `TensorCircuit` [78] and

Bloch sphere visualizations are plotted with the help from `QuTip` [79]. The computation of the Wasserstein distance, on the other hand, is performed by the Python library `POT` [80].

In Fig. 9, we show the training history of loss function in generating cluster state ensemble close to $|0,0\rangle$, whose corresponding performance is in Fig. 3 (b) in the main text. The fluctuation in the training history of every denoising step is due to the random measurement in each training steps. In sample generation with optimized denoising PQC, the fluctuation is comparably small to the mean.